The Astrophysical Journal, 659:1777–1783, 2007 April 20

MODELING OF THE HELIOSPHERIC INTERFACE, MAGNETIC FIELD, AND COSMIC-RAY TRANSPORT

S. E. S. Ferreira and M. S. Potgieter
Unit for Space Physics, School of Physics, North-West University, 2520 Potchefstroom, South Africa

and

K. Scherer
Institut für Theoretische Physik, Lehrstuhl IV: Weltraum- und Astrophysik, Ruhr-Universität Bochum, D-44780 Bochum, Germany
Received 2006 August 7; accepted 2006 November 30

ABSTRACT

Magnetized flow and cosmic-ray transport in the local astrosphere are studied. A hybrid numerical model is used to calculate the heliospheric interface, the heliospheric magnetic field, and cosmic-ray modulation. Assuming that the transport parameters scale inversely proportional to the magnetic field, the amplification of the field in the inner heliosheath results in a sudden decrease of these parameters over the shock. This, together with our model calculations showing the compressed and heated solar wind flow is not divergence-free in the postshock region, results in effective adiabatic acceleration of cosmic-ray particles in the heliosheath. In particular, the peak of the computed anomalous particles is not at the shock but some distance into the inner heliosheath, where this region becomes populated with relatively high intensities of heated anomalous particles. However, this effect is largely dependent on the values of the transport parameters in the heliosheath. It is also shown that an improvement in the kinematically transported heliospheric magnetic field leads to a significantly different spatial distribution of cosmic rays compared to a Parker model.

Subject headings: cosmic rays — solar wind — Sun: magnetic fields

Online material: color figures

1. INTRODUCTION

The expanding solar wind determines the heliosphere, a region filled with the solar wind plasma in the local interstellar medium (LISM). Inside this astrosphere, a transition is found where the supersonic solar wind decreases to subsonic speeds, creating a shock. The recent crossing (Krimigis et al. 2003; McDonald et al. 2003; Decker et al. 2005; Stone et al. 2005; Webber 2005) of this termination shock (TS) by the *Voyager 1* spacecraft has renewed interest in modeling, e.g., different plasma fluids (Holzer 1989; Suess 1990; Pauls & Zank 1996, 1997; Fahr et al. 2000; Scherer & Fahr 2003a, 2003b; Zank & Müller 2003; Izmodenov et al. 2005; Borrmann & Fichtner 2005), the heliospheric magnetic field (HMF; Florinski et al. 2003; Pogorelov et al. 2006), and the cosmic-ray (CR) intensities (Florinski et al. 2003; Ferreira & Scherer 2004, 2006; Langner & Potgieter 2005; Potgieter & Langner 2005; Ball et al. 2005) found in this region.

Of primary importance to the transport of CRs in the heliosphere is the coupling of the transport parameters to the background HMF and magnetic turbulence (e.g., Bieber et al. 1994; Schlickeiser 1999; Burger et al. 2000; Stawicki 2005a, 2005b). Also influencing the CR distribution are the geometry of the modulation volume and TS (Florinski et al. 2003; Ferreira et al. 2004; Ferreira & Scherer 2004; Langner & Potgieter 2005; Scherer & Ferreira 2005a; Ball et al. 2005) and propagating diffusion barriers (Burlaga et al. 1993; Potgieter & Le Roux 1994; le Roux & Fichtner 1999; Ferreira & Potgieter 2004; Ndiitwani et al. 2005; Scherer & Ferreira 2005b). See Potgieter (1998), Zank (1999), Ferreira & Potgieter (2004), and Fichtner (2005) for reviews.

To describe CR modulation, numerical transport models of increasing complexity have been developed since the early 1970s (Fisk 1976; Kota & Jokipii 1983; Potgieter & Moraal 1985; Jokipii 1986; le Roux & Potgieter 1990; Hattingh & Burger 1995; Steenberg & Moraal 1996; Zhang 1999; Gil & Alania 2001; Langner & Potgieter 2005). Almost all these models solved the Parker (1965) transport equation with predefined parameters including the solar wind flow, boundary and shock geometry, magnetic field, etc. Only recently have these models been adapted to calculate CR modulation in a realistically calculated heliosphere. This was done either by using a pressure approach (le Roux & Fichtner 1999; Fahr et al. 2000; Scherer & Fichtner 2004; Borrmann & Fichtner 2005), where the transport equation is averaged over momentum, or by including energy changes (Florinski et al. 2003; Ferreira et al. 2004; Scherer & Ferreira 2005a; Ball et al. 2005; Ferreira & Scherer 2006; Langner et al. 2006), where acceleration and cooling of particles can be computed.

In this work we utilize our existing hybrid numerical model (Scherer & Ferreira 2005a; Ferreira & Scherer 2006) to compute the interaction of the solar wind, the LISM, neutral hydrogen, and pickup ions (PUIs) to calculate the heliospheric interface. Newly added to the model is the calculation of the HMF in the kinematic approximation (see also Pogorelov et al. 2004 for three-dimensional MHD computations). The computed flow profiles and magnetic field are then inserted into a transport part that calculates CR transport and acceleration in this realistic heliosphere.

First, we will briefly compare computed anomalous cosmic ray (ACR) intensities using a Parker spiral (Parker 1958) in the transport model to intensities computed by solving the Faraday induction equation kinematically, assuming that the plasma velocity field is given and disregarding magnetic stresses in the conservation laws for different species. Such a comparison can be of value to authors (Langner & Potgieter 2005; Potgieter & Langner 2005; Caballero-Lopez et al. 2004) who still use the Parker equation when studying cosmic-ray modulation in the inner heliosheath, and also explains differences from our previous work (Ferreira et al. 2004; Scherer & Ferreira 2005a; Ferreira & Scherer 2006) using now a more correct treatment of the magnetic field. We should clearly mention that the kinematic approach used here and the self-consistent treatment of all five

species allows us to model, e.g., ACR and Galactic cosmic-ray (GCR) transport and acceleration over a solar cycle and beyond. Other models, such as that of Ball et al. (2005), can locally model the CR flux and globally model the full 3D MHD system or, like that of Pogorelov et al. (2006), put the emphasis on the global heliospheric structures, including the current sheet.

Furthermore, we will illustrate how different transport parameters result in different CR distributions in the outer heliosphere. For low-energetic ACRs and under the assumption that the diffusion parameters are inversely proportional to the magnitude of the HMF, our model predicts that the ACR distribution is not a maximum at the TS but a few AU beyond, as observations seem to indicate (Decker et al. 2005; Stone et al. 2005). In the postshock region for the compressed and heated solar wind, $\nabla \cdot \boldsymbol{V} < 0$ and adiabatic acceleration of CR particles can occur. This effect is further increased because of the amplification of the HMF (Nerney et al. 1993; Washimi & Tanaka 1996; Linde et al. 1998; Zank 1999; Florinski et al. 2003), which results in very small diffusion parameters in this region. To illustrate this, we will show different ACR modulation scenarios that correspond to the assumption that adiabatic acceleration (heating, $\nabla \cdot \boldsymbol{V} < 0$), cooling ($\nabla \cdot \boldsymbol{V} > 0$), and no energy changes ($\nabla \cdot \boldsymbol{V} = 0$) occur in the heliosheath. The latter two are theoretical cases artificially included in the model. As shown by Langner et al. (2006) this parameter can have a significant effect on cosmic-ray modulation.

Finally, we will show that by increasing the diffusion coefficients fewer particles are adiabatically accelerated in the heliosheath as well as at the termination shock. Therefore, current and future measurements from the two *Voyager* spacecraft may significantly contribute to our understanding of the acceleration of these particles in the heliosheath region and will give new insights into the transport coefficients. The observed intensity profiles of ACRs by the *Voyager* spacecraft can be used to indirectly determine the radial dependence of the solar wind speed in the inner heliosheath.

2. HYBRID MODEL

The model used in this work is 2D axisymmetric, allowing us to treat two independent variables, and has three parts. In the first part the interactions between various fluids are computed to obtain the heliospheric interface. The plasma flow is then used in a magnetic part where the induction equation is solved. The flow profiles and magnetic field are then used in a transport part where CR transport and acceleration can be computed. See Scherer & Ferreira (2005a) for details. Before discussing this model we want to point out that in order to save on computational resources we have, for the purpose of this work, neglected the back-reaction of the HMF (Florinski et al. 2003), as well as the ACR and GCR pressure (see le Roux et al. 2000; Fichtner 2001; Florinski et al. 2004 for the effects of these particles on the TS geometry) on the proton fluid. We also solve our model in (r, θ) coordinates (see also Scherer & Ferreira 2005a; Ferreira & Scherer 2006). This significantly reduces computational resources so that dynamic processes can be included later. Solving CR transport in this plane, compared to, e.g., the equatorial plane, has additional advantages in that simulated particle drifts (Hattingh & Burger 1995) and perpendicular diffusion in the polar direction can be included. Both processes significantly influence CR transport (Potgieter 1999; Burger et al. 2000).

2.1. *Hydrodynamics*

The size and features of the heliosphere are mainly determined by the interaction of the solar wind and the LISM (see Holzer 1989; Zank 1999 for reviews). However, the LISM is partly ionized, with half of it consisting of protons and half of hydrogen. This interstellar neutral H can exchange charge with the LISM plasma (especially in the nose, where the plasma has been decelerated and heated), creating a subpopulation. If the charge exchange mean free path is sufficiently small in the region of decelerated LISM flow, a wall of neutral H will form in the upstream direction of the heliospheric nose (see Linsky & Wood 1996 for observations). Neutral H atoms that cross the heliopause into the heliosphere can also experience charge exchange with the very hot subsonic plasma downstream of the TS. This neutral H can transport heat from the heliosheath into the LISM. In addition, neutral H will also experience charge exchange with the supersonic solar wind (see Baranov & Malama 1995; Zank et al. 1996; Fahr et al. 2000 for modeling results).

An example of the heliospheric structure, in terms of number density, is shown in Figure 1. Shown on the left is the proton density, n_p, and on the right the neutral H density, $n_{\rm H}$. For this calculation we assumed $n_p = 6$ and 0.1 cm^{-3} in the solar wind and LISM, respectively, while for the neutral H in the LISM we have $n_{\rm H} = 0.1$ cm^{-3}. The solar wind speed, with temperature 100,000 K, is 400 km s^{-1} at all latitudes, and the LISM speed is 26 km s^{-1} with temperature 8000 K.

The top panels of Figure 1 show the density as a gray scale in the meridional plane, and the bottom panels show radial profiles in the nose (*solid line*), pole (*dashed line*), and tail (*dash-dotted line*) directions. The inclusion of neutral H in the model reduces the size of the heliosphere because of the removal of momentum from the supersonic solar wind by charge exchange (see Zank et al. 1996; Fahr et al. 2000). The important heliospheric structures such as the TS, heliopause, hydrogen wall, and even bow shock are clearly visible. Furthermore, the heliosphere is asymmetrical because of the movement through the LISM and is also elongated toward the poles (e.g., Pauls & Zank 1996, 1997; Scherer & Ferreira 2005a; Fahr et al. 2000). Note that we computed a heliosphere typical of solar maximum conditions where there is no fast solar wind over the poles. However, for solar minimum conditions the elongation of the heliosphere will be more pronounced because of the latitudinal variation of the solar wind momentum flux (Phillips et al. 1995; McComas et al. 2001, 2003).

Another important fluid affecting the heliospheric geometry and included in our hydrodynamic description is the so-called pickup ions (PUIs). These ions, created out of the interaction of neutral H with the surrounding plasma, are of considerable importance because they remove both momentum and energy from the solar wind flow. The solar wind gets decelerated, therefore reducing the ram pressure and subsequently the size of the heliosphere. The initial PUI population is unstable, generating magnetic turbulence which can scatter both PUIs and CRs. See Zank (1999) for an overview.

To model these interactions we solve the following set of Euler equations,

$$\frac{\partial}{\partial t}\rho_i + \nabla \cdot (\rho_i \boldsymbol{u}_i) = Q_{p,i}, \tag{1}$$

$$\frac{\partial}{\partial t}(\rho_i \boldsymbol{u}_i) + \nabla \cdot (\rho_i \boldsymbol{u}_i \boldsymbol{u}_i + P_i \boldsymbol{I}) = \boldsymbol{Q}_{m,i}, \tag{2}$$

$$\frac{\partial}{\partial t}\left(\frac{\rho_i}{2}\boldsymbol{u}_i^2 + \frac{P_i}{\gamma_i - 1}\right) + \nabla \cdot \left(\frac{\rho_i}{2}\boldsymbol{u}_i^2 \boldsymbol{u}_i + \frac{\gamma_i \boldsymbol{u}_i P_i}{\gamma_i - 1}\right) = Q_{e,i}, \tag{3}$$

which describe the balance of mass, momentum, and energy of the protons in the solar wind and LISM ($i = p$) and the neutral H population ($i = H$), to calculate the heliospheric geometry and plasma flow. For the PUIs ($i = \mathrm{PUI}$) only the equation for the

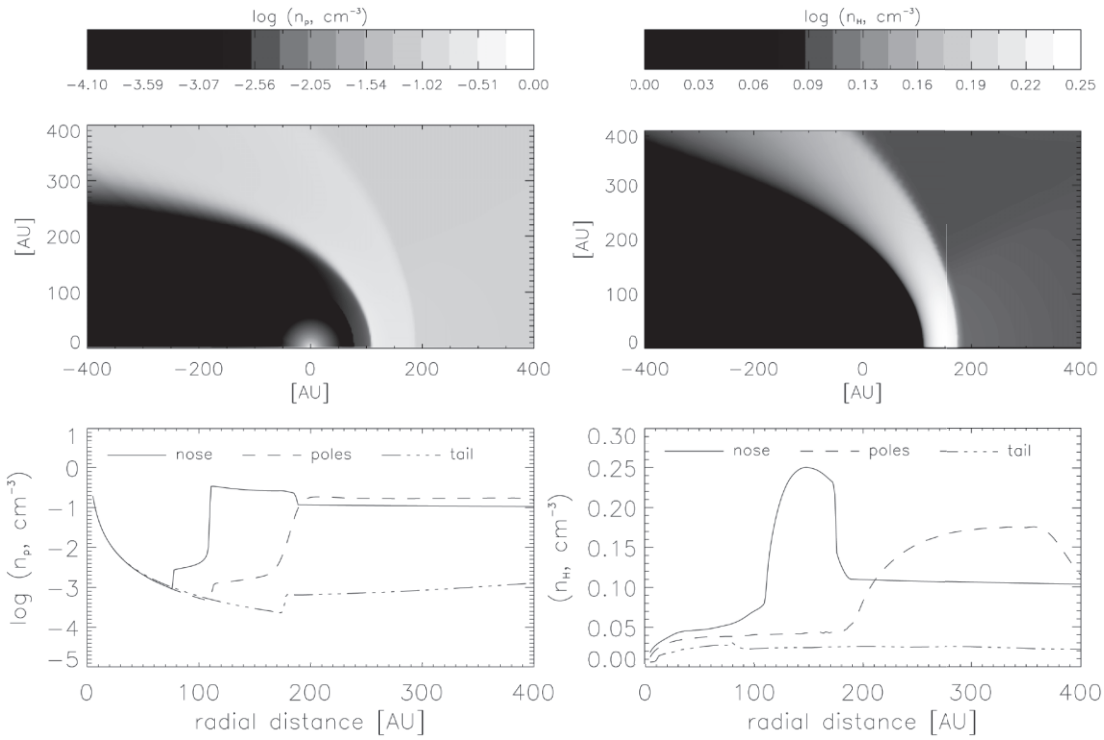

FIG. 1.—Computed heliosphere. Shown on the left is the solar wind–LISM proton density, n_p, and on the right the neutral H density, $n_{\rm H}$, in particles per cubic centimeter. The top panels shows the density as a gray scale in the meridional plane, and the bottom panels the radial profiles in the nose (*solid line*), pole (*dashed line*), and tail (*dash-dotted line*) directions. [*See the electronic edition of the Journal for a color version of this figure.*]

conservation of mass is taken into account. The fluid quantities are the mass density ρ_i, velocity $\boldsymbol{u}_i$, and pressure P_i, while $\boldsymbol{I}$ denotes the unity tensor and γ_i the adiabatic indices of the components. The time is t, and Q_i denote the sources related to the interaction between various species. For a full description see Fahr et al. (2000) and Scherer & Ferreira (2005a). The additional two species are ACRs and GCRs, which are computed with a transport equation, described below.

2.2. *Heliospheric Magnetic Field*

To calculate the heliospheric magnetic field $\boldsymbol{B}$ we start with Faraday's law, which gives

$$\nabla \times \boldsymbol{E} = -\frac{\partial \boldsymbol{B}}{\partial t}, \tag{4}$$

with $\boldsymbol{E}$ the electric field. Neglecting the electric force (infinite conductivity limit) gives $\boldsymbol{E} = -\boldsymbol{v} \times \boldsymbol{B}$, and by inserting this into Faraday's law we get

$$\frac{\partial \boldsymbol{B}}{\partial t} + \nabla \times (\boldsymbol{v} \times \boldsymbol{B}) = 0. \tag{5}$$

We solve this equation in an advection step to obtain the radial B_r, azimuthal B_ϕ, and polar B_θ components. For example, for B_ϕ in spherical coordinates,

$$\frac{\partial B_\phi}{\partial t} = \frac{1}{r}\left\{\frac{\partial}{\partial r}\left[r\left(v_\phi B_r - v_r B_\phi\right)\right] - \frac{\partial}{\partial \theta}\left(v_\theta B_\phi - v_\phi B_\theta\right)\right\}, \tag{6}$$

with v_r, v_θ, and v_ϕ the different components of the flow speed. To solve equation (5) we set a boundary condition $B_\phi = 0.5$ nT (obtained from the Parker [1958] equation) at an artificial boundary at 10 AU. The components B_r, B_θ, and B_ϕ are then calculated with a constraining step added to ensure that no magnetic monopoles occur, $\nabla \cdot \boldsymbol{B} = 0$ (Pen et al. 2003; Trac & Pen 2003). To solve these equations we use a simplified version of the high-resolution finite volume method described by LeVeque (2002). Furthermore, we assume $\boldsymbol{B} = 0$ beyond the heliopause. Note that the structure of the heliopause in the tail region is model dependent (Fahr et al. 1986) varying between a closed or open heliopause. Our model computes an open heliopause in the tail region, with an outflow condition at 800 AU to save on computational resources.

Because the spiral field above and its extension into the heliosheath results in extraordinary large diffusion coefficients (Jokipii & Kota 1989; Jokipii et al. 1995; Potgieter 1999), a modified field B_m with only an azimuthal component (Florinski et al. 2003) was added to the system of magnetic field equations. For this we solve the convection equation,

$$\frac{\partial B_m}{\partial t} = \nabla \cdot B_m \boldsymbol{v}. \tag{7}$$

The total field inside the heliosphere is then given by

$$B^2 = B_r^2 + B_\theta^2 + B_\phi^2 + B_m^2. \tag{8}$$

The top panel of Figure 2 shows the computed unmodified B (eq. [8] without B_m) in the meridional plane as a contour plot. The inset shows the radial profile in the nose (*solid line*), pole (*dashed line*), and tail (*dash-dotted line*) directions of the heliosphere. As expected for the equatorial regions and inside the TS, $B \propto 1/r$ with some minor deviation due to the effect of PUIs and neutral H. For the poles, $B \propto 1/r^2$ for a large part of the inner heliosphere where the field is almost completely radial, while for

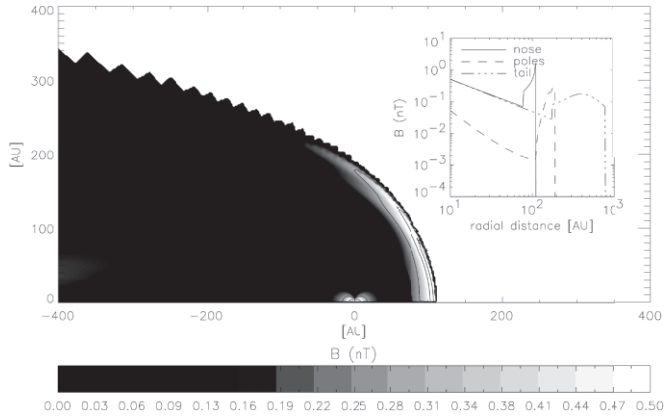

FIG. 2.—Computed heliospheric magnetic field in the meridional plane solving the induction equation in the kinematic approximation without any modifications, shown as a contour plot. The inset shows the radial profile of the field in the nose (*solid line*), pole (*dashed line*), and tail (*dash-dotted line*) directions of the heliosphere. [*See the electronic edition of the Journal for a color version of this figure*.]

the outer heliospheric polar regions the azimuthal contribution dominates resulting in $B \propto 1/r$.

An important feature in Figure 2 is the existence of a highly amplified field in the heliosheath. This is known as the Axford-Cranfill effect (Cranfill 1971; Axford 1972), where a magnetic wall emerges from the amplification of the B_ϕ component caused by the flow deceleration and the convection to higher latitudes (Nerney et al. 1993; Washimi & Tanaka 1996; Linde et al. 1998; Zank 1999; Florinski et al. 2003). As shown, over the shock B abruptly increases by a factor corresponding to the compression ratio. Further into the heliosheath a steady increase is computed due to the decelerating plasma. Beyond the heliopause $\boldsymbol{B} = 0$ due to the boundary condition imposed here. We neglect the interstellar magnetic field and possible diamagnetic effects induced by the PUIs (Fahr & Scherer 2005).

The top panel in Figure 3 shows the radial profiles of the HMF (computed by solving the induction equation) for the heliospheric nose (*solid line*), poles (*dashed line*), and tail (*dash-dotted line*). These are compared to a Parker field with the computed flow values (obtained from the hydrodynamic part) as input. The latter is shown by the dotted lines in all three directions. The bottom panel is similar, except that $v_\theta = 0$ in equation (6) when Faraday's law was solved. This comparison is done because these two models result in different ACR spatial distributions, as we will show below. Note further that Figure 3 shows that especially in the inner heliosheath the Parker spiral is no longer valid and a more sophisticated approach is needed. Our kinematic approach is a first step in that direction. See, e.g., Pogorelov et al. (2006) for a more sophisticated 3D MHD approach.

Comparing the solution of the induction equation to the Parker field (Fig. 3, *top*) illustrates that for regions inside the TS both approaches result in the same field. This is to be expected because the computed solar wind speed was used as input for the Parker field (Scherer & Ferreira 2005a; Ferreira & Scherer 2006). In the heliopause, solving Faraday's law results in a slightly smaller B in the nose and a larger B at the poles because of the amplification and transport of B_ϕ to higher latitudes. This feature is not included in the Parker approach. By setting $v_\theta = 0$ in equation (6) the induction equation now results in a B which is almost the same as the Parker field because there is now no convection of B_ϕ to higher latitudes and therefore no magnetic wall in these regions.

Figure 4 is similar to Figure 2 except in this case the modified field (*inset*) was added to the field. This modification became

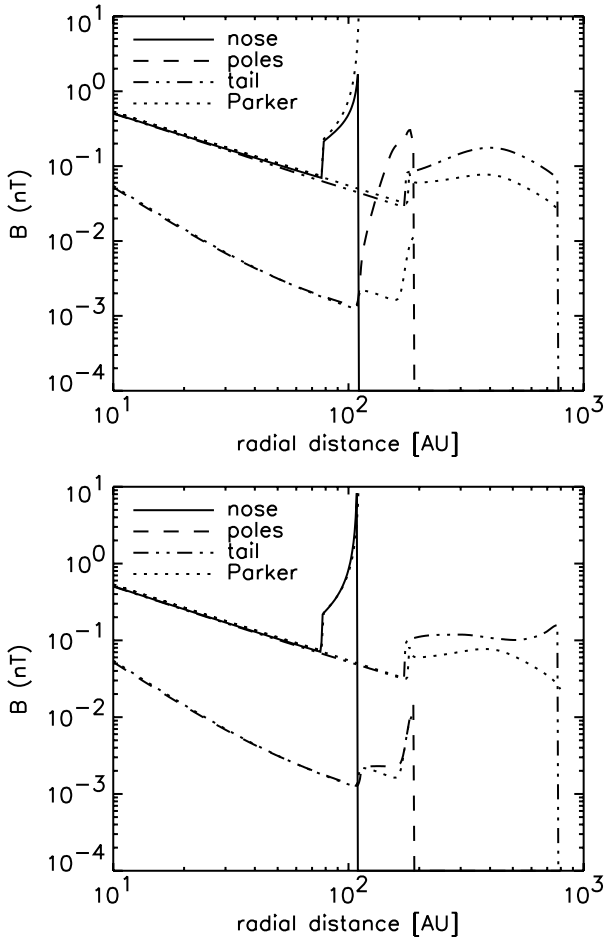

FIG. 3.—*Top:* Computed (solving the induction equation) unmodified field compared to the Parker field (using the computed solar wind speed as input). *Bottom:* Same as the top, except $v_\theta = 0$ in eq. (6) when Faraday's induction equation was solved. Computations are shown in the nose (*solid line*), poles (*dashed line*), and tail (*dash-dotted line*). The dotted line shows the Parker solution.

necessary because of the drift velocities in the polar regions that have been shown in traditional drift modulation models (e.g., Jokipii & Kota 1989; Haasbroek & Potgieter 1995; Burger & Sello 2005). To include this field we assumed that $B_m = 0.1$ nT at the boundary at 10 AU and solved the advection equation for the modified field in the rest of the heliosphere. Note that the modified field only has an azimuthal component (see Florinski et al. 2003). Comparing Figure 4 to Figure 2 illustrates that the addition of the modified field affects the total field only in a small cone around the polar axis and only where the unmodified field became very small, e.g., in the upwind direction close to the shock.

2.3. *Cosmic-Ray Transport*

Once calculated, the heliospheric geometry, plasma flow, and HMF are used in the kinetic transport part, based on implicitly solving the Parker (1965) transport equation,

$$\frac{df}{dt} = \nabla \cdot (\mathbf{K} \cdot \nabla f) - \boldsymbol{V} \cdot \nabla f + \frac{1}{3}(\nabla \cdot \boldsymbol{V}) \frac{\partial f}{\partial \ln P} + Q, \quad (9)$$

to calculate ACR and GCR transport in two spatial dimensions (r, θ), where θ is the polar angle, r is the radial distance, and t is the time, directly from the LISM (meaning no Dirichlet conditions at the heliopause; see also Florinski et al. 2003). Furthermore, P is the rigidity, Q is any source of CRs inside the heliosphere, $\boldsymbol{V}$ is the

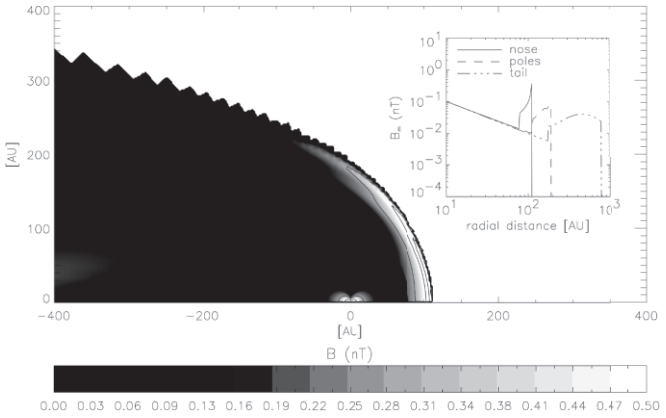

FIG. 4.—Same as Fig. 2, but with the modified field B_m added to the total field. The modified field is shown in the inset. [*See the electronic edition of the Journal for a color version of this figure.*]

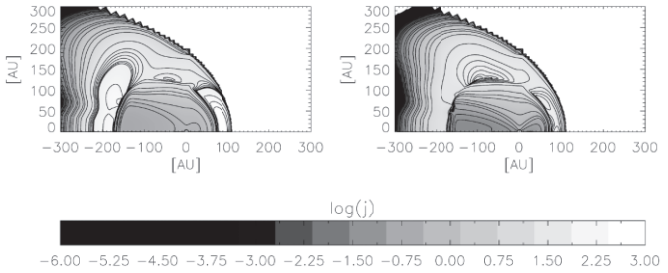

FIG. 5.—Computed 10 MeV ACR proton differential intensities, j, in units of particles m^{-2} s^{-1} sr^{-1} MeV^{-1}. Computations were done without drifts. The left panel shows computations done using the Parker model for the HMF when the transport equation is solved. Details can be found in Scherer & Ferreira (2005a). The right panel shows ACR computations when the induction equation was solved to obtain the HMF and then used when solving the transport equation. [*See the electronic edition of the Journal for a color version of this figure.*]

solar wind velocity (as calculated by the hydrodynamic part), **K** is the diffusion tensor, and f is the omnidirectional distribution function with differential intensity $j = P^2 f$ in units of particles m^{-2} s^{-1} sr^{-1} MeV^{-1}. This equation includes all the major transport processes: diffusion, convection, drifts, and energy changes.

In this work we focus on the ACR distribution in the outer heliosphere. For this population, a monoenergetic source is specified at the TS (Steenberg & Moraal 1996; Steenberg 1998; Caballero-Lopez et al. 2004). The injection efficiency is chosen from observational constraints, e.g., to produce realistic ACR spectra (Ferreira & Scherer 2006) compared to observations. As reported by Langner (2004) the corresponding solutions are independent of the injection energy as long as it is lower than the TS cutoff energy. Note that the numerical grid was chosen so that the grid spacing was smaller than the diffusive length scale of the low-energy ACRs (see e.g., Florinski et al. 2004).

The two most important transport processes in equation (9) are diffusion and drifts. The corresponding coefficients can be found in the diffusion tensor **K**; the coefficients of special interest are

$$\kappa_{rr} = \kappa_{\parallel} \cos^2 \psi + \kappa_{\perp r} \sin^2 \psi, \tag{10}$$

$$\kappa_{\theta\theta} = \kappa_{\perp\theta}, \tag{11}$$

$$\kappa_A = \frac{\beta P}{3B}, \tag{12}$$

giving the radial and polar diffusion and drifts, respectively, with heliospheric magnetic field B and spiral angle ψ. In these equations, $\kappa_{\parallel}$ is diffusion parallel to the heliospheric magnetic field, $\kappa_{\perp r}$ is perpendicular diffusion in the radial direction, and $\kappa_{\perp\theta}$ is perpendicular diffusion in the polar direction. The spiral angle ψ is defined as

$$\tan \psi = \frac{\Omega (r - R_{\odot}) \sin \theta}{V(t)}, \tag{13}$$

where Ω is the angular speed of the Sun and $R_{\odot}$ is the solar radius; ψ depends on the solar wind speed. Therefore, any temporal changes caused by the solar cycle variability in the supersonic solar wind speed $V(t)$ also has an effect on the radial diffusive transport and drift processes because of the dependence on the spiral angle. The procedure to calculate the cosmic-ray spectra in the heliosphere, e.g., how to solve equation (9) numerically, was described by Scherer & Ferreira (2005a). Note that in this work we concentrate on solar maximum conditions and therefore neglect drift effects. As shown by Ferreira & Potgieter (2004) drifts should be scaled down considerably toward solar maximum to even no drifts when calculating realistic charge-sign–dependent modulation.

In this work we assumed $K_{\parallel}$ for protons as calculated by Teufel & Schlickeiser (2002; damping model) for the inner heliosphere. This is then scaled as $B_0(\theta)/B(r, \theta)r$, with B_0 the value of the magnetic field at Earth and B either the Parker spiral field or the magnetic field found by solving the induction equation. Dividing by r results in K_{rr} almost independent of distance for regions inside the shock. The effect of the sudden deceleration of the solar wind plasma to subsonic speeds at the TS, the amplification of B in the heliosheath, and the effect on the diffusion parameters can be seen in Figures 2–4. Concerning $K_{\perp}$ and $K_{\parallel}$, current theoretical work includes Bieber et al. (2004), Shalchi et al. (2004), Minnie et al. (2005), and Stawicki (2005a, 2005b). However, for simplicity we will assume that K_{rr} scales as $K_{\parallel}$ (le Roux et al. 1999; Giacalone & Jokipii 1999; Qin et al. 2002) and that $K_{rr} = 0.15K_{\parallel}$ and $K_{\theta\theta} = 0.3K_{\parallel}$.

Figure 5 shows the 10 MeV computed ACR proton distribution in the meridional plane without drifts. The left panel shows computations that can be compared to previous computations done by Scherer & Ferreira (2005a) and Ferreira & Scherer (2006). In this approach the HMF was calculated using the computed solar wind flow as input to the Parker equation. Details can be found in the above cited two papers. The right panel shows ACR computations done using a more realistic magnetic field by solving the induction equation in the kinematic approximation.

Apart from the small differences inside the TS, the largest differences in the computed ACR proton intensities, corresponding to the different field models, are found at the TS and especially at the heliospheric poles. First, for the flow obtained by solving the Euler equations together with Faraday's law, fewer ACRs are accelerated to this energy (10 MeV) in the equatorial regions, compared to a Parker field. This is because of the larger K_{rr}, for which there is less amplification of B in the heliopause in the equatorial regions. When solving the induction equation, some of the B_{ϕ} components are transported toward higher latitudes, a feature that does not occur in the Parker field model.

Second, more ACR protons are found at higher latitudes when Faraday's law is solved than for the Parker field. As mentioned earlier a significant fraction of B_{ϕ} (and the modified field B_m) is transported from lower latitudes resulting in a significant enhancement of B in the polar regions of the heliopause. The result is a large decrease of the transport parameters across the shock and in the heliopause, resulting in very effective acceleration. Note that as reported by Scherer & Ferreira (2005a) ACRs are also

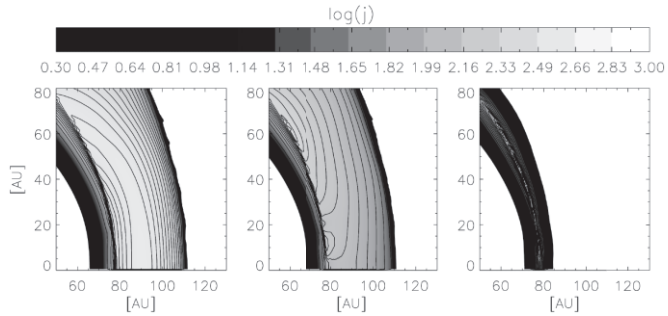

FIG. 6.—Computed 10 MeV ACR proton differential intensities, j, in units of particles m^{-2} s^{-1} sr^{-1} MeV^{-1}. The left panel corresponds to a scenario where adiabatic heating of ACRs occurs, with $\nabla \cdot \boldsymbol{V} < 0$. For the middle panel $\nabla \cdot \boldsymbol{V} = 0$, and for the right panel it was assumed that $\nabla \cdot \boldsymbol{V} > 0$ and the ACRs are cooled. The latter two are theoretical scenarios. [*See the electronic edition of the Journal for a color version of this figure.*]

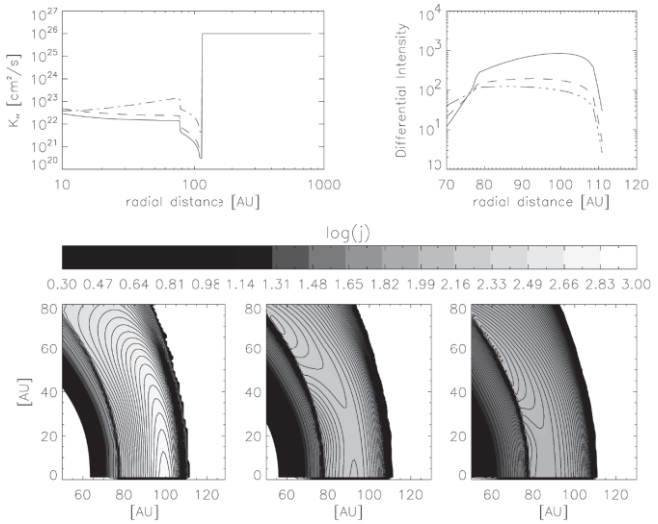

FIG. 7.—Different values of K_{rr} (*top left*) and corresponding computed 10 MeV ACR proton differential intensities, j (*top right*), in the equatorial plane in the heliospheric nose. The bottom three panels show the spatial ACR distributions in the heliospheric nose due to the different values of K_{rr}. The bottom left panel shows solutions corresponding to the solid line, the bottom middle panel to the dashed line, and the bottom right panel to the dash-dotted line. Note that only intensities above 10 particles m^{-2} s^{-1} sr^{-1} MeV^{-1} are shown. [*See the electronic edition of the Journal for a color version of this figure.*]

easily accelerated in the polar regions toward he heliospheric tail. This is in the region of the so-called tornado alley, where our hydrodynamic model computes a divergence of the solar wind that approaches the value in the equatorial regions. With the amplification of B in the polar regions due to the transport of B_m and B_ϕ toward higher latitudes, this effect is now enhanced.

Figure 6 shows three computed scenarios for the 10 MeV proton ACR distribution in the outer heliosphere. For simplicity and because we concentrate on solar maximum conditions, we assume no drifts (see Langner & Potgieter 2005; Potgieter & Langner 2005 for GCR computations). The left panel depicts calculations where the computed solar wind flow from the hydrodynamic model is used as input to the transport part. For this scenario the postshocked solar wind plasma is compressed and heated, resulting in $\nabla \cdot \boldsymbol{V} < 0$. Although these values are much smaller than values at the TS, the compressed flow does result in very effective adiabatic acceleration of ACRs in the heliosheath (Florinski et al. 2004; Langner et al. 2006). For this scenario a spacecraft crossing the shock will measure a gradual increase in particle intensities where the peak in the computed ACR profile is a few AU away from the shock. In addition, the whole heliosheath seems filled with these low-energy particles.

For the middle panel in Figure 6 it was assumed that no energy changes occur in the heliosheath, setting $\nabla \cdot \boldsymbol{V} = 0$. As shown, the intensity of the ACRs is significantly reduced, with the maximum intensity occurring at the TS. For the right panel it was assumed that adiabatic cooling occurs, setting $\nabla \cdot \boldsymbol{V} > 0$. The ACRs are now strongly modulated on both sides of the shock, and a definite peaked profile at the TS is computed. These graphs illustrate the role of adiabatic heating and/or cooling on ACRs in the outer heliosphere. In a future paper these aspects will be investigated in more detail.

Next the effect of different K_{rr} on ACR intensities at and beyond the shock is shown for the scenario where adiabatic heating occurs. Figure 7 shows in the top left panel different K_{rr} and in the top right panel the corresponding computed 10 MeV ACR proton intensities in the equatorial plane of the heliospheric nose. The bottom three panels show the ACR distribution in the nose corresponding to the different K_{rr}. The contour plot shown in the bottom left panel corresponds to the solid line, the bottom middle panel to the dashed line, and the bottom right panel to the dash-dotted line. We assume that in the LISM isotropic diffusion exists with $K_{rr} = K_{\theta\theta} = 10^{26}$ cm^2 s^{-1}, which is somewhat lower than usually used (e.g., Hartquist & Morfill 1994; Florinski et al. 2003). However, for the purpose of this work only ACRs are studied, and we assume that these particles are swept away outside the heliopause (Scherer & Ferreira 2005a) with the intensity set to zero. The full effect of the transport of accelerated ACRs in particular into the interstellar medium will be reported in a future paper.

Figure 7 shows that, depending on the magnitude of K_{rr}, the ACRs can have either a peaked profile at the shock or an almost constant radial dependence in the heliosheath or even an increasing profile as shown in the top right panel (Langner & Potgieter 2005; Potgieter & Langner 2005; Caballero-Lopez et al. 2004). As shown by the contour plots, for the smallest K_{rr} (*solid line and bottom left*) the particles are very effectively accelerated at the shock, and the largest intensity enhancement is not found at the shock but at ~100 AU due to the adiabatic acceleration in the heliosheath. For the middle panel, the peaked profile is found at ~90 AU, and the intensity of the accelerated ACRs is also lower, as expected. For the bottom right panel, the computed intensity is the lowest, with the highest intensity found at the shock, and a peaked profile is subsequently computed. Therefore, current and future observations from the *Voyager* spacecraft may provide valuable insights into the acceleration of these particles in the heliosheath region and the influence of the transport parameters on this effect.

3. SUMMARY AND CONCLUSIONS

In this work we presented a hybrid numerical model to compute the interaction of the solar wind, the LISM, neutral hydrogen, and pickup ions (PUIs). Newly added to the model is the kinematic calculation of the HMF via Faraday's law. The flow profiles and magnetic field are then inserted into a transport part which calculates cosmic-ray transport and acceleration in this realistic heliosphere.

For low-energy ACRs and under the assumption that the diffusion parameters are inversely proportional to the HMF, our model predicts that the ACR distribution does not peak at the TS but a few AU away. In the postshock region the solar wind is compressed and heated, resulting in $\nabla \cdot \boldsymbol{V} < 0$, and adiabatic acceleration of CR particles can occur. Although $\nabla \cdot \boldsymbol{V}$ in the heliosheath is much smaller than at the TS, the integrated effect on the

acceleration of ACRs over the heliosheath region results in this region being filled with accelerated particles of relatively high intensities. This effect, however, is strongly dependent on the magnitude of the diffusion parameters. Furthermore, when it was assumed that no energy changes occur in the heliosheath, which is divergence-free flow, the intensity of the ACRs was significantly reduced with the maximum intensity occurring at the TS. For the interesting theoretical scenario where adiabatic cooling may occur, ACRs are strongly modulated on both sides of the shock and a definite peaked profile at the TS is computed. The effect of adiabatic acceleration may, however, be significantly reduced by assuming large transport coefficients.

We have also shown briefly that by using the HMF obtained by solving Faraday's law as input in a transport model, fewer ACRs are accelerated compared to, e.g., a Parker field. This is because we assumed that our diffusion parameters are inversely proportional to B. For the kinematic approach the amplification of B in the heliosheath in the equatorial regions is less where some of the B_ϕ component was transported toward higher latitudes. Increased numbers of ACRs are also found at higher latitudes than in the equatorial regions when the induction equation is solved. This is because a significant fraction of B_ϕ (and the modified field B_m) is transported from lower latitudes resulting in an enhancement of B in the polar regions of the heliosheath. The result is a large decrease of the transport parameters across the shock and in the heliopause, resulting in very effective adiabatic acceleration.

We wish to thank Horst Fichtner, Ulrich Langner, Bernd Heber, and Jasper Snyman for valuable discussions. The authors are grateful for financial support granted to them by the South African National Research Foundation under grant 2053475 and the Deutsche Forschungsgemeinschaft in the frame of the project "Heliotrigger" (Fa 97/28-1) and "Heliocauses" (Fi 706/6-1).

REFERENCES

Axford, W. I. 1972, in Solar Wind, ed. C. P. Sonett, P. J. Coleman, & J. M. Wilcox (NASA SP-308; Washington: NASA), 598
Ball, B., Zhang, M., Rassoul, H., & Linde, T. 2005, ApJ, 634, 1116
Baranov, V. B., & Malama, Y. G. 1995, J. Geophys. Res., 100, 14755
Bieber, J. W., Matthaeus, W. H., Shalchi, A., & Qin, G. 2004, Geophys. Res. Lett., 31, 10805
Bieber, J. W., Matthaeus, W. H., Smith, C. W., Wanner, W., Kallenrode, M.-B., & Wibberenz, G. 1994, ApJ, 420, 294
Borrmann, T., & Fichtner, H. 2005, Adv. Space Res., 35, 2091
Burger, R. A., Potgieter, M. S., & Heber, B. 2000, J. Geophys. Res., 105, 27447
Burger, R. A., & Sello, P. C. 2005, Adv. Space Res., 35, 643
Burlaga, L. F., McDonald, F. B., & Ness, N. F. 1993, J. Geophys. Res., 98, 1
Caballero-Lopez, R. A., Moraal, H., & McDonald, F. B. 2004, J. Geophys. Res., 109, 5105
Cranfill, C. 1971, Ph.D. thesis, Univ. California (San Diego)
Decker, R. B., Krimigis, S. M., Roelof, E. C., Hill, M. E., Armstrong, T. P., Gloeckler, G., Hamilton, D. C., & Lanzerotti, L. J. 2005, Science, 309, 2020
Fahr, H. J., Kausch, T., & Scherer, H. 2000, A&A, 357, 268
Fahr, H. J., Neutsch, W., Grzedzielski, S., Macek, W., & Ratkiewicz-Landowska, R. 1986, Space Sci. Rev., 43, 329
Fahr, H. J., & Scherer, K. 2005, J. Geophys. Res. Space Phys., 110, 2103
Ferreira, S. E. S., & Potgieter, M. S. 2004, Adv. Space Res., 34, 115
Ferreira, S. E. S., Potgieter, M. S., & Scherer, K. 2004, ApJ, 607, 1014
Ferreira, S. E. S., & Scherer, K. 2004, ApJ, 616, 1215
———. 2006, ApJ, 642, 1256
Fichtner, H. 2001, Space Sci. Rev., 95, 639
———. 2005, Adv. Space Res., 35, 512
Fisk, L. A. 1976, J. Geophys. Res., 81, 4646
Florinski, V., Zank, G. P., Jokipii, J. R., Stone, E. C., & Cummings, A. C. 2004, ApJ, 610, 1169
Florinski, V., Zank, G. P., & Pogorelov, N. V. 2003, J. Geophys. Res., 108, 1
Giacalone, J., & Jokipii, J. R. 1999, ApJ, 520, 204
Gil, A., & Alania, M. V. 2001, in Proc. 27th Int. Cosmic Ray Conf. (Hamburg), 3725
Haasbroek, L. J., & Potgieter, M. S. 1995, Space Sci. Rev., 72, 385
Hartquist, T. W., & Morfill, G. E. 1994, Ap&SS, 216, 223
Hattingh, M., & Burger, R. A. 1995, Adv. Space Res., 16, 213
Holzer, T. E. 1989, ARA&A, 27, 199
Izmodenov, V., Malama, Y., & Ruderman, M. S. 2005, A&A, 429, 1069
Jokipii, J. R. 1986, J. Geophys. Res., 91, 2929
Jokipii, J. R., & Kota, J. 1989, Geophys. Res. Lett., 16, 1
Jokipii, J. R., Kóta, J., Giacalone, J., Horbury, T. S., & Smith, E. J. 1995, Geophys. Res. Lett., 22, 3385
Kota, J., & Jokipii, J. R. 1983, ApJ, 265, 573
Krimigis, S. M., Decker, R. B., Hill, M. E., Armstrong, T. P., Gloeckler, G., Hamilton, D. C., Lanzerotti, L. J., & Roelof, E. C. 2003, Nature, 426, 45
Langner, U. W. 2004, Ph.D. thesis, Potchefstroomse Univ. Christelike Hoër Onderwys
Langner, U. W., & Potgieter, M. S. 2005, ApJ, 630, 1114
Langner, U. W., Potgieter, M. S., Fichtner, H., & Borrmann, T. 2006, J. Geophys. Res. Space Phys., 111, 1106
le Roux, J. A., & Fichtner, H. 1999, J. Geophys. Res., 104, 4709
le Roux, J. A., Fichtner, H., & Zank, G. P. 2000, J. Geophys. Res., 105, 12557
le Roux, J. A., & Potgieter, M. S. 1990, ApJ, 361, 275
le Roux, J. A., Zank, G. P., & Ptuskin, V. S. 1999, J. Geophys. Res., 104, 24845
LeVeque, R. J. 2002, Finite Volume Methods for Hyperbolic Problems (Cambridge: Cambridge Univ. Press)
Linde, T. J., Gombosi, T. I., Roe, P. L., Powell, K. G., & Dezeeuw, D. L. 1998, J. Geophys. Res., 103, 1889
Linsky, J. L., & Wood, B. E. 1996, ApJ, 463, 254
McComas, D. J., Elliott, H. A., Schwadron, N. A., Gosling, J. T., Skoug, R. M., & Goldstein, B. E. 2003, Geophys. Res. Lett., 30, 24
McComas, D. J., Goldstein, R., Gosling, J. T., & Skoug, R. M. 2001, Space Sci. Rev., 97, 99
McDonald, F. B., Stone, E. C., Cummings, A. C., Heikkila, B., Lal, N., & Webber, W. R. 2003, Nature, 426, 48
Minnie, J., Burger, R. A., Parhi, S., Matthaeus, W. H., & Bieber, J. W. 2005, Adv. Space Res., 35, 543
Ndiitwani, D. C., Ferreira, S. E. S., Potgieter, M. S., & Heber, B. 2005, Ann. Geophys., 23, 1061
Nerney, S., Suess, S. T., & Schmahl, E. J. 1993, J. Geophys. Res., 98, 15169
Parker, E. N. 1958, ApJ, 128, 664
———. 1965, Planet. Space Sci., 13, 9
Pauls, H. L., & Zank, G. P. 1996, J. Geophys. Res., 101, 17081
———. 1997, J. Geophys. Res., 102, 19779
Pen, U.-L., Arras, P., & Wong, S. 2003, ApJS, 149, 447
Phillips, J. L., et al. 1995, Geophys. Res. Lett., 22, 3301
Pogorelov, N. V., Zank, G. P., & Ogino, T. 2004, ApJ, 614, 1007
———. 2006, ApJ, 644, 1299
Potgieter, M. S. 1998, Space Sci. Rev., 83, 147
———. 1999, Adv. Space Res., 23, 449
Potgieter, M. S., & Langner, U. W. 2005, Adv. Space Res., 35, 554
Potgieter, M. S., & Le Roux, J. A. 1994, ApJ, 423, 817
Potgieter, M. S., & Moraal, H. 1985, ApJ, 294, 425
Qin, G., Matthaeus, W. H., & Bieber, J. W. 2002, Geophys. Res. Lett., 29, 7
Scherer, K., & Fahr, H. J. 2003a, Ann. Geophys., 21, 1303
———. 2003b, Geophys. Res. Lett., 30, 17
Scherer, K., & Ferreira, S. E. S. 2005a, Ap&SS Trans., 1, 17
———. 2005b, A&A, 442, L11
Scherer, K., & Fichtner, H. 2004, A&A, 413, L11
Schlickeiser, R. 1999, A&A, 351, 382
Shalchi, A., Bieber, J. W., & Matthaeus, W. H. 2004, ApJ, 604, 675
Stawicki, O. 2005a, Adv. Space Res., 35, 547
———. 2005b, ApJ, 624, 178
Steenberg, C. D. 1998, Ph.D. thesis, Potchefstroomse Univ. Christelike Hoër Onderwys
Steenberg, C. D., & Moraal, H. 1996, ApJ, 463, 776
Stone, E. C., Cummings, A. C., McDonald, F. B., Heikkila, B. C., Lal, N., & Webber, W. R. 2005, Science, 309, 2017
Suess, S. T. 1990, Rev. Geophys., 28, 97
Teufel, A., & Schlickeiser, R. 2002, A&A, 393, 703
Trac, H., & Pen, U.-L. 2003, PASP, 115, 303
Washimi, H., & Tanaka, T. 1996, Space Sci. Rev., 78, 85
Webber, W. R. 2005, J. Geophys. Res. Space Phys., 110, 10103
Zank, G. P. 1999, Space Sci. Rev., 89, 413
Zank, G. P., & Müller, H.-R. 2003, J. Geophys. Res., 108, 7
Zank, G. P., Pauls, H. L., Williams, L. L., & Hall, D. T. 1996, J. Geophys. Res., 101, 21639
Zhang, M. 1999, ApJ, 510, 715